Journal of Materials Chemistry A

ROYAL SOCIETY OF CHEMISTRY

PAPER

View Article Online
View Journal | View Issue

Cite this: J. Mater. Chem. A, 2025, 13, 8526

Transformative chelation pathways unveiling NiMOF-LDH hybrids on MgO for high-efficiency photocatalysis†

Mohammad Aadil,[a] Ananda Repycha Safira,[a] Mohammad Alkaseem,[b] Taekjib Choi [c] and Mosab Kaseem *[a]

The significant influence of the sequential addition of EDTA on the growth of NiMOF on an inorganic surface (MgO) was studied. By precisely controlling the sequence of EDTA introduction, we successfully engineered two distinct structures: a highly crystalline and robust NiMOF coating and a NiMg layered double hydroxide (LDH) structure. When EDTA was applied directly to the MgO surface prior to NiMOF formation, a well-adhered, high-performance NiMOF coating was achieved. In contrast, simultaneous or post EDTA introduction resulted in the formation of a NiMg LDH layer. This peculiar behavior, observed for the first time, indicates that EDTA critically influences NiMOF crystallization, either facilitating the formation of a robust NiMOF coating or triggering its breakdown, leading to NiMg LDH formation. Photocatalytic degradation experiments using an organic dye (rhodamine B) and an antibiotic (tetracycline) were conducted to evaluate the effectiveness of the coatings. The results demonstrated that the EDTA addition prior to NiMOF formation yielded the most efficient photocatalyst, degrading 99.2% of Rhd B within just 25 minutes, approximately 6% higher than the next best performer, the NiMOF–EDTA sample. Furthermore, the EDTA–NiMOF coating achieved 90.7% degradation of TC in 120 minutes, significantly surpassing the NiMOF–EDTA sample with a 40% increase in efficiency. In contrast, samples featuring the NiMg LDH structure exhibited markedly lower photocatalytic activity, particularly in the degradation of TC, implying the superior performance of the EDTA–NiMOF complex. This superior photocatalytic activity can be attributed to the higher density of active sites and enhanced adsorption properties of the EDTA–NiMOF complex. This research underscores how synthesis parameters influence the structure and function of hybrid materials, providing insights for designing durable, efficient photocatalysts for environmental remediation.

Received 24th December 2024
Accepted 11th February 2025

DOI: 10.1039/d4ta09131k

rsc.li/materials-a

1. Introduction

Hybrid materials represent a unique class of substances that combine the best of both inorganic and organic components at the molecular or nanoscale level. These materials offer an exciting blend of the properties typically associated with their individual components, such as the structural robustness of inorganic materials and the tunability and versatility of organic systems. As a result, hybrid materials are finding increasing applications in various fields, including catalysis, energy storage, drug delivery, environmental remediation, and more. Some of the most widely studied hybrid materials include metal–organic frameworks (MOFs),[1–4] layered double hydroxides (LDHs),[5,6] perovskites,[7–9] and covalent organic frameworks (COFs).[10,11]

MOFs are crystalline materials formed by the coordination of metal ions or clusters with organic linkers.[12] Due to their highly ordered structures and tunable porosity, MOFs have attracted significant interest for applications in gas storage,[13,14] catalysis,[15–18] and drug delivery.[19,20] The porous nature of MOFs allows for high surface areas and accessibility to active sites, making them ideal candidates for adsorption and separation processes. For instance, Sankar *et al.* synthesized mono- and bimetallic MOFs, with a fibrous structure, using a simple wet chemical approach, which were subjected to overall water splitting, resulting in low voltage to achieve the oxygen and hydrogen evolution reaction.[21] Moreover, Safira *et al.* generated a paper-like structured coating of Co-MOF in the presence of PVP, on a MgO surface, to achieve 99.74% degradation of 4-nitrophenol within 5 minutes.[22]

[a]Corrosion and Electrochemistry Laboratory, Department of Nanotechnology and Advanced Materials Engineering, Sejong University, Seoul 05006, Republic of Korea. E-mail: mosabkaseem@sejong.ac.kr

[b]Owlstone Medical, Cambridge CB4 0GJ, UK

[c]Hybrid Materials Research Center, Department of Nanotechnology and Advanced Materials Engineering, Sejong University, Seoul 05006, Republic of Korea

† Electronic supplementary information (ESI) available. See DOI: https://doi.org/10.1039/d4ta09131k

LDHs, often referred to as anionic clays, are layered materials composed of positively charged metal hydroxide layers and intercalated anions between them.[23] LDHs have been extensively studied for their ion-exchange capabilities,[24,25] environmental remediation properties,[26–30] and use as precursors for mixed metal oxides.[31,32] Their lamellar structure offers ion exchange properties, and the composition of the metal cations can be varied to introduce catalytic activity or other functional properties. For example, novel $Cu_xNi_yFe_z$-LDHs were synthesized by Wen *et al.*, for selective catalytic reduction with propylene (SCR-C_3H_6) to achieve exceptional performance.[33]

Ethylenediaminetetraacetic acid (EDTA) is a powerful chelating agent widely recognized for its ability to bind strongly to metal ions through multiple coordination sites.[34,35] Its structure, featuring four carboxyl groups and two amine groups, allows it to form stable complexes with various metal ions, making it essential in applications such as water treatment,[36] industrial cleaning,[37] pharmaceuticals,[38] and food preservation.[39] In materials science, EDTA plays a key role in directing the synthesis of hybrid materials such as metal–organic frameworks (MOFs) and layered double hydroxides (LDHs), influencing their structural and functional properties, particularly in catalysis and environmental remediation. For instance, EDTA was utilized to synthesize EDTA-based Ni–Co-MOF nanospheres by Khan *et al.*, to achieve an exotic redox behavior with a specific capacity of 450.67 C g^{-1} at 3 mV s^{-1} and 474.56 C g^{-1} at 1 A g^{-1}.[40]

In this study, we examine the dual role of EDTA in driving the formation of two distinct hybrid materials: a highly crystalline, porous MOF structure and a layered LDH structure. By varying the sequence and conditions of EDTA introduction, we show how this chelating agent can either promote the assembly of a robust MOF or facilitate the transition to a NiMg LDH phase. The synthesis begins with the formation of a magnesium oxide (MgO) layer on the surface of an AZ31 magnesium alloy using high voltage. Our research focuses on how these EDTA-induced transformations influence the photocatalytic performance of the materials, specifically targeting the degradation of organic pollutants such as rhodamine B and tetracycline. Bulk coatings, rather than powder photocatalysts, were employed to avoid binding with degradation products in the later stages of catalysis. This study aims to elucidate the relationship between the structural characteristics and functional capabilities of these hybrid materials, advancing the design of more efficient and versatile photocatalysts for targeted applications.

2. Experimental and theoretical details

2.1. Materials

Sodium phosphate (Na_3PO_4), potassium hydroxide (KOH), sodium hydroxide (NaOH), nickel(II) nitrate ($Ni(NO_3)_2 \cdot 6H_2O$), terephthalic acid ($C_8H_6O_4$), dimethyl formamide (C_3H_7NO), ethyl alcohol (C_2H_6O), isopropyl alcohol (C_3H_8O), ethylenediaminetetraacetic acid ($C_{10}H_{16}N_2O_8$), benzoquinone ($C_6H_4O_2$), rhodamine B ($C_{28}H_{31}ClN_2O_3$), tetracycline ($C_{22}H_{24}N_2O_8$), and deionized water were used for the fabrication and photocatalytic evaluation of the functional coatings. The functional coating was formed on a bulk sample, which was prepared by sizing the magnesium alloy (AZ31) to dimensions of $10 \times 10 \times 2$ mm^3, which was polished with emery papers up to 2000 grit, cleaned with ethanol, and subsequently dried.

2.2. Fabrication of the inorganic layer

The formation of the inorganic surface was carried out in a glass beaker equipped with a cooling and stirring system. The electrolyte used consisted of 10 g L^{-1} Na_3PO_4, and 2 g L^{-1} KOH. An AC power source (ACP-1010) was used to employ a current density of 100 mA cm^{-2}, with a frequency of 60 Hz and a coating time of 600 s. After the process, a porous, inorganic layer is formed on the surface of the substrate. This sample was named MgO, as the major constituent of this inorganic layer is magnesium oxide.

2.3. Post modification

For the post modification of the inorganic layer to transform it into a functional coating, a nickel-based metal organic framework (Ni-MOF) was synthesized in combination with EDTA. Herein, the inorganic layer was first modified with 10 mmol of EDTA under hydrothermal conditions, where the parameters were set to be 80 °C for 3 hours, and the pH of the solution was set to 10 by dropwise addition of 1 mol NaOH solution. After the surface is treated with EDTA, further modification is performed where 50 mmol TPA and 50 mmol $Ni(NO_3)_2 \cdot 6H_2O$ were dissolved in 35 mL DMF and 5 mL ethanol. This solution was stirred for 30 minutes before placing it in an autoclave at a temperature of 120 °C for 6 hours, and the resultant sample was named 'EDTA–NiMOF'. To observe the effect of the arrangement of the aforementioned process, Ni-MOF was formed first on the inorganic layer, which was then modified with EDTA, and this sample was named 'NiMOF–EDTA'. Furthermore, the combined effect of EDTA and Ni-MOF was also observed in which the solution was prepared using the same concentration as that in the aforementioned process; however, because this is a one-step method, the parameter of hydrothermal treatment was set at 120 °C for 6 hours; the subsequent sample was named 'NiMOF + EDTA'. A schematic representation of the formation of the porous MgO surface and the post-treatment process is depicted in Fig. 1.

2.4. Microstructural characterization

The microstructural analysis was performed in order to get information of the functional coating. Microimaging was performed using a field emission scanning microscope (FESEM, SU8010 HITACHI), and the elemental analysis was simultaneously performed using energy dispersion spectroscopy (EDX). To observe the functional group present in the coating, Fourier transformed infrared spectroscopy (FTIR, 380 Nicolet, ATR mode) was performed at the wavenumber between 500–4000 cm^{-1}. X-ray diffraction (XRD, Panalytical) and X-ray photoelectron spectroscopy (XPS, PHI 5000 ULVACPHI) were

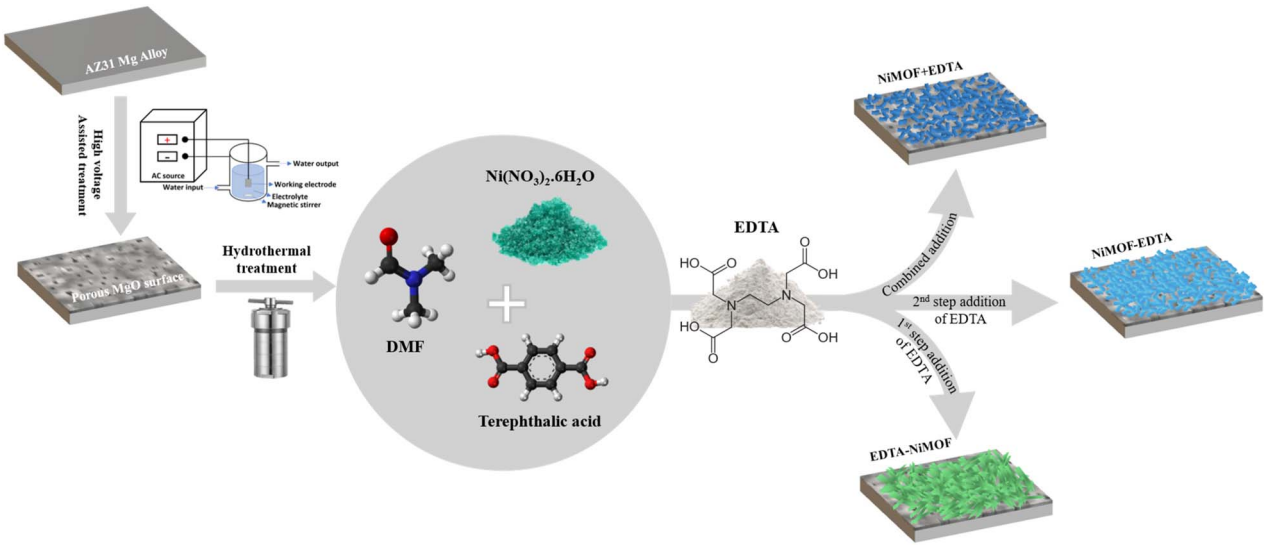

Fig. 1 Schematic representation of the experimental procedure for synthesizing MgO, NiMOF + EDTA, NiMOF–EDTA, and EDTA–NiMOF coatings.

performed to analyze the crystalline constituents and the chemical composition, respectively, of the coatings.

2.5. Photocatalytic evaluation

Photocatalytic degradation of the organic dye (Rhd B) and an antibiotic (TC) was conducted to evaluate the impact of sequential EDTA addition on the material's functionality. The photodegradation experiments were performed in the presence of hydrogen peroxide (H_2O_2), which served as a reaction initiator. For photocatalytic degradation, a UV-light source (Ultra Vitalux OSRAM lamp, 300 W) at a distance of 20 cm and room temperature (30 °C) emitting 45 μW cm^{-2} as measured at 297 nm is utilized to illuminate the dye within the glass beaker. Solutions containing 20 mg L^{-1} of Rhd B and 20 mg L^{-1} of TC were prepared, with 40 mL of each solution placed in separate glass beakers. To initiate the photocatalytic process, 0.2 mL of H_2O_2 was added to each solution. The catalysts were placed in the solutions under dark conditions for 60 minutes to stabilize the experimental conditions.

The progress of the degradation was monitored using a UV-Vis spectrometer (Agilent Cary 5000) to measure the absorbance peak intensities. For Rhd B, 3 mL were extracted every 5 minutes, while for TC, samples were taken every 20 minutes. The degradation efficiency was calculated using the following equation:

$$\text{Degradation efficiency}(\%) = \frac{C_0 - C}{C_0} \times 100 \quad (1)$$

where C_0 denotes the original intensity of Rhd B or TC and C denotes the intensity after a certain time. To determine the reaction kinetics of the photocatalytic process, the following equations were employed.

$$\text{Pseudo first order kinetics: } \ln C_0 - k_1 \quad (2)$$

$$\text{Pseudo second order kinetics: } 1/C = 1/C_0 - k_2 t \quad (3)$$

't' represents the time relative to the concentration, k_1 is the pseudo-first-order rate constant (min^{-1}), and k_2 is the pseudo-second-order rate constant (L mg^{-1} min^{-1}). Moreover, a mixture of these solutions was also photodegraded using the same methods. UV-Vis diffuse reflectance spectroscopy (UV-DRS) was employed to investigate the light absorption properties and to measure the band gap of the catalyst using the Tauc method.

2.6. Theoretical calculations

The proposed structures of the complexes were generated using the 3D modeling capabilities of GaussView 6.0 software, followed by optimization using the Gaussian 09W software package. For these theoretical calculations, the density functional theory (DFT) method was employed, specifically utilizing the Becke, 3-parameter, Lee–Yang–Parr (B3LYP) functional combined with the 6-31G basis set. The optimized energies were calculated and compared to provide theoretical insight into the stability and formation of the complexes. Additionally, the adsorption energies of the complex of the best sample with both Rhd B and TC were calculated to assess the role of adsorption energy in influencing the photocatalytic performance.

3. Results and discussion

3.1. Morphological analysis

Fig. 2 shows the FESEM images at different magnifications of MgO and the different coatings formed on it, *i.e.*, combination coating of EDTA and NiMOF (NiMOF + EDTA) in a one-step process, sequential coating in which NiMOF was formed first and EDTA was formed in the second step to obtain NiMOF–EDTA, and another sequential coating in which we inversed the procedure to obtain EDTA–NiMOF.

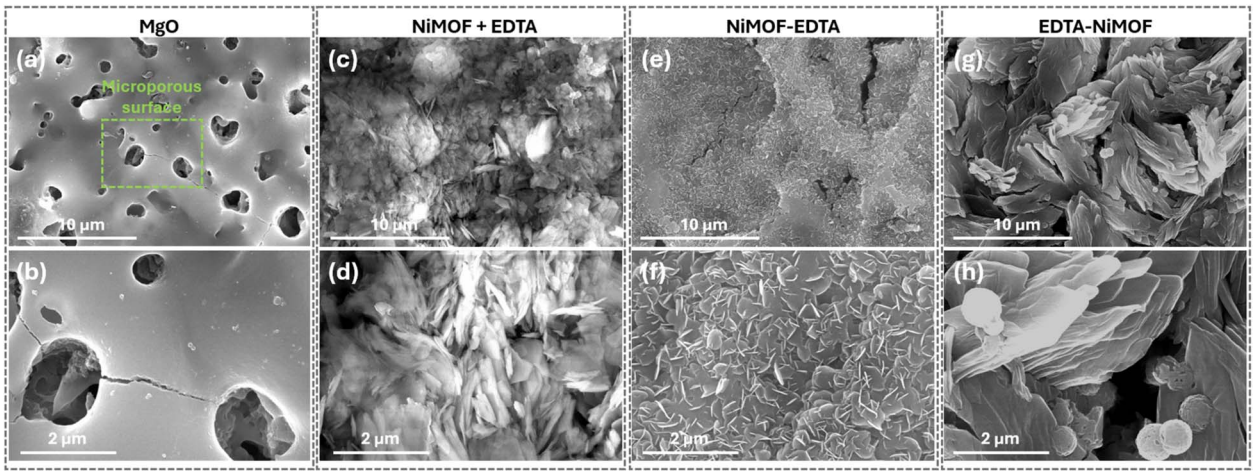

Fig. 2 Surface morphology and magnified images of (a and b) MgO, (c and d) NiMOF + EDTA, (e, f) NiMOF–EDTA, and (g and h) EDTA–NiMOF.

The MgO sample, shown in Fig. 2(a and b), displayed numerous well-distributed micropores and microcracks, which were formed due to the plasma discharges induced by high voltage. During plasma discharges, micro-explosions of molten oxide and hydrogen gas are produced, forming an inorganic metal oxide layer on the surface. The formation mechanism reactions that take place during the inorganic layer formation are shown in eqn (4)–(8).

$$2H_2O \rightarrow 2H_2 + O_2 \quad (4)$$

$$Mg \rightarrow Mg^{2+} + 2e^- \quad (5)$$

$$Na_3PO_4 \rightarrow 3Na^+ + PO_4^{3-} \quad (6)$$

$$2Mg + O_2 \rightarrow 2MgO \quad (7)$$

$$Mg^{2+} + 2PO_4^{3-} \rightarrow Mg_3(PO_4)_2 \quad (8)$$

This inorganic layer, characterized by its porous surface, provides a large surface area and facilitates the post-modification process by offering numerous nucleation sites.[22] To enhance the number of active sites and create a stable, photocatalytically active coating, post-modification was employed. The combined one-step modification of NiMOF and EDTA resulted in a coating with an irregular flaky structure, indicating that some complex between NiMOF and EDTA was formed, as shown in Fig. 2(c and d). This structure is likely due to the coordination of the carboxylic acid groups from terephthalic acid (TPA) and the anionic oxygen atoms from EDTA with the Ni ions.

The framework structures of the MOFs, both before and after EDTA treatment, were investigated to determine whether EDTA participates in coordination and contributes to framework formation. As shown in Fig. S1(a and b),† the surface morphology of NiMOF grown on the MgO surface exhibits a microcrystalline structure. Following the formation of NiMOF, treatment with EDTA resulted in a flaky structure, as presented in Fig. 2(e and f), which was presumed to be a layered double hydroxide (LDH) formed in the presence of Mg^{2+} and Ni^{2+} ions. This speculation of LDH formation was confirmed during further characterization. The second-step addition of EDTA was essential for the formation of NiMg LDH, as it provided the necessary hydroxide ions (OH^-), which came from the pH adjustment using NaOH.

The surface morphology of MgO treated with EDTA is presented in Fig. S1(c and d),† showing that EDTA formed a complex with the entire surface, effectively functionalizing the MgO surface. Subsequently, the formation of NiMOF in the second step resulted in a scaly structure, as shown in Fig. 2(g and h), attributable to the effective formation of the NiMOF coating facilitated by the initial EDTA treatment. It is hypothesized that the anionic oxygen atoms from EDTA initially form an organic–inorganic complex with the MgO surface. During the subsequent NiMOF formation, the excess anionic oxygen from the EDTA serves as nucleation sites, promoting the nucleation and growth of NiMOF on the surface.

To gain further insight into the surface functionalization, chemical composition was obtained through EDX analysis. The main constituents of the inorganic surface are magnesium (36.79%), oxygen (49.98%), and phosphorus (12.26%), due to the formation of MgO and $Mg_3(PO_4)_2$ during high-voltage electrolysis, as shown in Fig. 3(a). The surface of NiMOF + EDTA displayed a fair spread of carbon (44.90%), oxygen (41.60%), nitrogen (2.09%), and nickel (9.63%), on top of the elements present on the MgO surface, as shown in Fig. 3(b). The approximately equal distribution of oxygen and carbon can be attributed to the one-step functionalization and the contribution from the NiMOF and EDTA complex. In the case of NiMOF–EDTA, the dominant element was oxygen (49.5%) due to the formation of the LDH structure, which is abundant in OH^- ions, as shown in Fig. 3(c). The presence of 6.42% nickel after flaky structure formation confirms the formation of NiMg LDH. Conversely, Fig. 3(d) shows that EDTA–NiMOF consists of 24.28% oxygen, significantly less than all other samples, as the oxygen from EDTA is sandwiched between MgO and NiMOF, forming a strong bond between these two layers. The

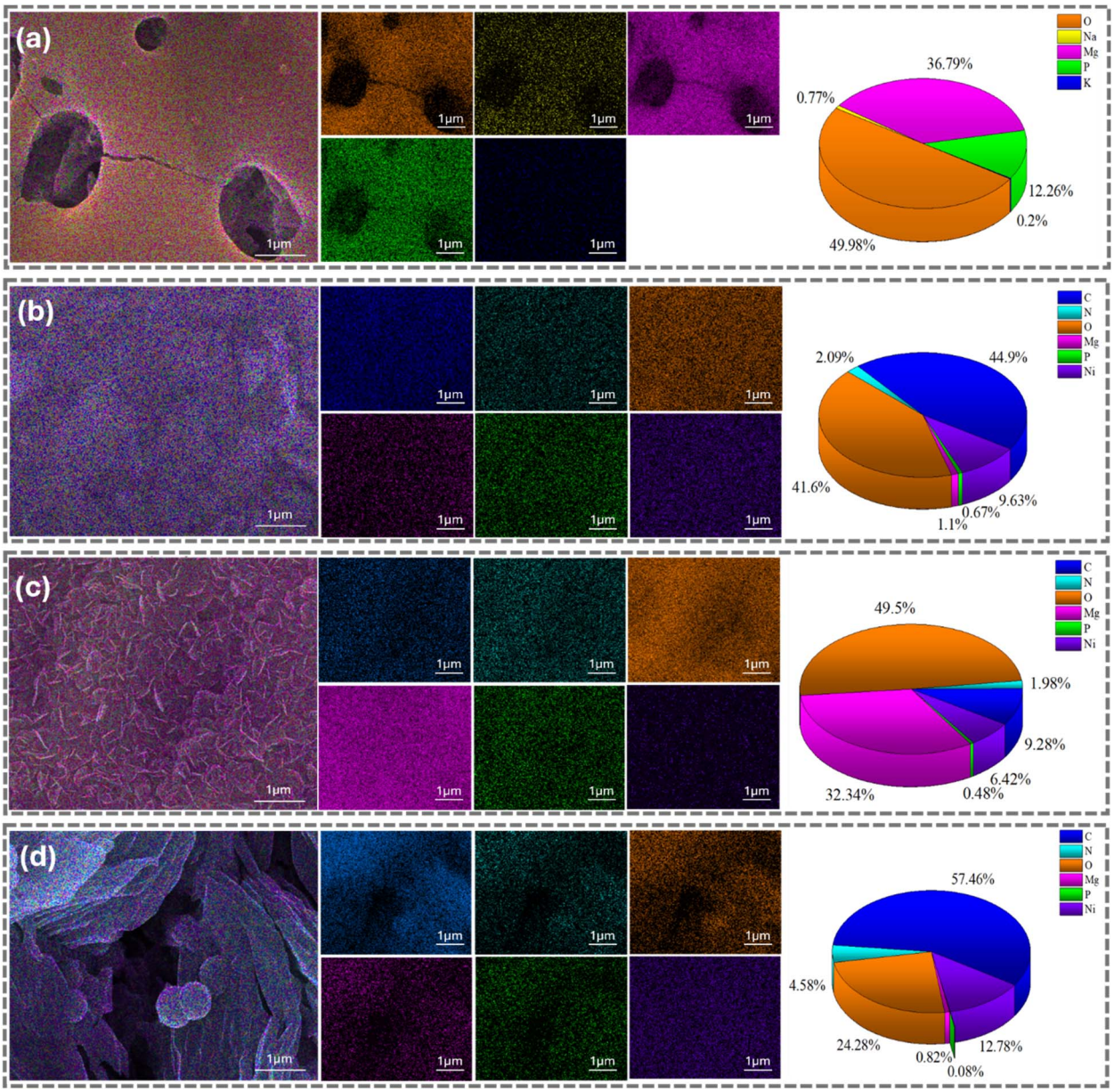

Fig. 3 EDX layered analysis of the magnified images, along with the individual elemental and their respective weight percentages of (a) MgO, (b) NiMOF + EDTA, (c) NiMOF–EDTA, and (d) EDTA–NiMOF.

percentages of nickel (12.78%) and nitrogen (4.58%) were significantly higher than in the previously discussed sample, suggesting the formation of a functional scaly MOF coating. It is interesting to note that the sequencing of the addition of EDTA plays a crucial role in the morphology of the structure formed.

3.2. Compositional analysis

Fig. 4(a) presents the FTIR spectrum of MgO, NiMOF + EDTA, NiMOF–EDTA, and EDTA–NiMOF, to assess the functional groups of the coatings. The absence of peaks for the MgO sample confirms that there are no functional groups present. Therefore, further discussion will contain information about all samples except the MgO sample. The adsorption band located between 3600–3000 cm^{-1} is mainly attributed to the stretching vibrations of –OH groups, indicating the presence of physically adsorbed water molecules on the surface. This is a common feature in all samples, suggesting the ubiquitous presence of moisture.[41] The peaks at 1597.6 cm^{-1} indicated the presence of C=C bonding present in the aromatic ring.[42] The shoulder peak at 1648.8 cm^{-1} in the EDTA–NiMOF sample is attributed to the carbonyl group, which was due to the presence of terephthalic acid which is assumed to be coordinated with nickel metal ions to form the MOF.[43] The peak present at 1498.8 could be attributed to the presence of the benzene ring,[44] and this peak reveals that there is an insignificant amount of benzene present in NiMOF + EDTA and NiMOF–EDTA, indicating that the MOF structure with terephthalic acid and nickel was not formed.

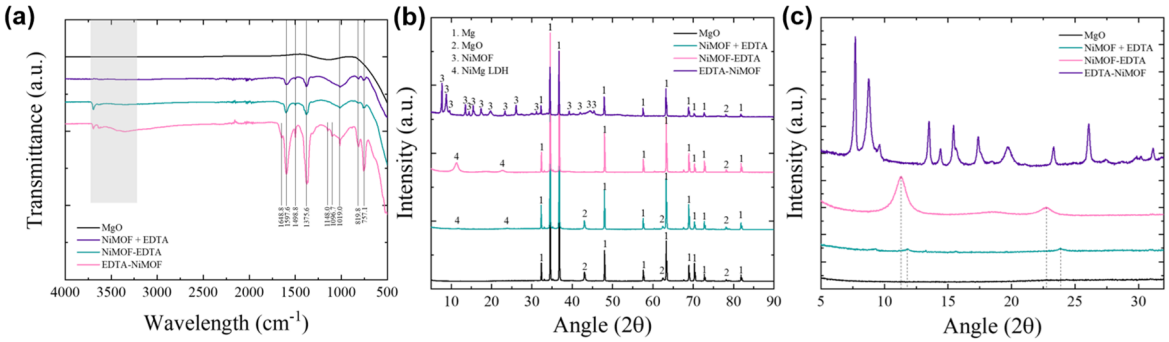

Fig. 4 (a) FTIR analysis and (b) XRD analysis for all samples, and (c) a magnified XRD pattern in the 5–35° range.

Moreover, a strong peak of C–N and C–O stretching was formed at 1735.6 cm^{-1} and 1019.0 cm^{-1}, respectively.[45,46] There are also small shoulder peaks in EDTA–NiMOF at 1148.0 and 1096.7 cm^{-1} which are attributed to C–O stretching. Furthermore, the peaks between 830 and 725 cm^{-1} are related to C–H vibration in the benzene ring.[46] There were no discrete peaks observed in relation to the MOF structure; therefore further characterization was performed.

Fig. 4(b) illustrates the XRD pattern of all the samples, over the angular range of 5–90° (2θ), in order to analyze the structural composition. Every sample displayed characteristic peaks of Mg (JCPDS # 00-035-0821) and MgO (JCPDS # 00-045-0946), arising from the substrate and the MgO coating formed during high-voltage electrolysis. In contrast, the peaks of $Mg_3(PO_4)_2$ could not be identified, because of its amorphous nature. Fig. 4(c) presents the magnified XRD pattern between 5–30° (2θ). Characteristic peaks of LDH were observed for NiMOF + EDTA and NiMOF–EDTA, which provides compelling evidence that the structure formed was related to NiMg LDH. It could be assumed that the sequential introduction of EDTA has a massive role in changing the NiMOF to a NiMg LDH structure. Previous reports on LDH formation in divalent systems[47,48] provide further validation for our findings. The property of EDTA as a chelating agent plays a crucial role in the observed structural transformations.[49,50] When EDTA is introduced in the first step, it binds strongly to the Ni^{2++} ions within the MOF structure, disrupting the original coordination between nickel ions and terephthalic acid (TPA). Simultaneously, the dissolution of MgO occurs, forming Mg^{2+} ions. At a pH of 10, maintained by the addition of NaOH, the solution contains a significant concentration of OH^- ions. These alkaline conditions favor the dissociation of the $Ni(EDTA)^{2-}$ complex, releasing free Ni^{2+} ions into the solution. The free Ni^{2+} ions, along with Mg^{2+} ions, then participate in the formation of the NiMg LDH structure.

$$NiMOF + EDTA \rightarrow Ni[EDTA]^{2-} + TPA \quad (9)$$

$$Ni[EDTA]^{2-} + 4OH^- \rightarrow Ni^{2+} + EDTA^{4-} + 4OH^- \quad (10)$$

$$MgO + H_2O \rightarrow Mg(OH)_2 \rightarrow Mg^{2+} + 2OH^- \quad (11)$$

$$xNi^{2+} + yMg^{2+} + (x + y + 2)OH^- \rightarrow Ni_xMg_y(OH)_{2(x+y)} \quad (12)$$

The smaller intensity and right-shifted XRD peaks observed in the NiMOF + EDTA sample, compared to the NiMOF–EDTA sample, can be attributed to differences in their formation processes. The one-step hydrothermal treatment in the presence of EDTA could result in less controlled crystallinity and variable stoichiometry, leading to lower peak intensities and reduced layer spacing. Conversely, the sequential process used for NiMOF–EDTA allows for more controlled formation, resulting in a higher crystallinity of the LDH structure, as evidenced by the more intense and correctly positioned XRD peaks. Additionally, the presence of the MgO peak in the NiMOF + EDTA sample, coupled with the significantly smaller peaks associated with NiMg LDH, suggests that the coating is thin and non-uniform. On the other hand, EDTA–NiMOF displayed a completely different set of peaks corresponding to MOF peaks. These MOF peaks have high intensity, and the peaks related to magnesium are comparably shorter for this sample, suggesting that the coating is thick, and fewer X-rays penetrated through the surface of the coating to reach the MgO surface. The significance of the sequence in which EDTA is added on the structural properties is clearly evident here.

Due to the negligible differences in the XPS spectra of the post-treated samples, only the high-resolution XPS spectra of Mg1s, Ni2p, C1s, O1s, and N1s elements for the EDTA–NiMOF sample are shown in Fig. 5. The full XPS survey, shown in Fig. 5(a), provides comprehensive information on all the elemental peaks present in the sample. Notably, the intensity of the Mg1s peak is significantly lower than that of other main elements, due to the limited penetration depth of X-rays, which do not extend more than 10 nm beneath the surface. However, deconvolution of the small Mg1s peak reveals three distinct peaks corresponding to Mg, $Mg_3(PO_4)_2$, and MgO at binding energies of ~1303.2 eV, ~1304.0 eV, and ~1304.7 eV, respectively. The Ni2p spectrum, presented in Fig. 5(c), displayed two main peaks corresponding to the $Ni2p_{3/2}$ and $Ni2p_{1/2}$ sublevels. Within the $Ni2p_{3/2}$ peak, two distinct subpeaks were identified at ~855.4 eV attributed to Ni^{2+}, and ~860.8 eV represents a satellite peak. Similarly, the $Ni2p_{1/2}$ peak exhibited two subpeaks at ~873.0 eV and ~878.9 eV, corresponding to Ni^{2+} and a satellite peak, respectively. The identification of these peaks supports the successful incorporation of Ni^{2+} into the synthesized structures, whether in the form of the Ni-MOF or the NiMg

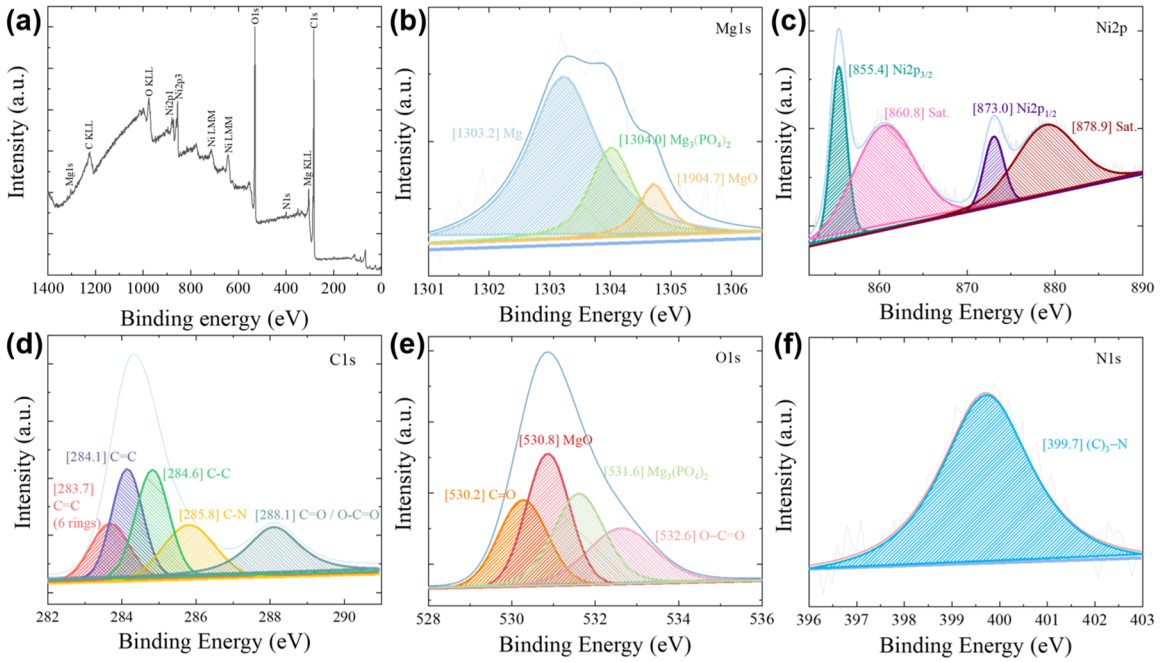

Fig. 5 XPS analysis of the EDTA–NiMOF sample: (a) full elemental survey, (b) Mg1s, (c) Ni2p, (d) C1s, (e) O1s, and (f) N1s spectra.

LDH. Fig. 5(d) displays the C1s XPS spectrum, where the deconvolution shows five subpeaks. Additionally, the C1s spectrum provided insights into the nature of the organic compounds used in forming the coatings. Peaks observed at ~283.7 eV and ~284.1 eV correspond to C=C bonds, indicating the presence of aromatic groups. The peak at around ~285.8 eV is attributed to C–C bonds, arising from the aliphatic carbon chains within the organic compounds. Furthermore, peaks at approximately ~285.8 eV and ~288.1 eV are indicative of C–N and C=O or O–C=O bonding, respectively. The O1s peaks shown in Fig. 5(e) confirm the presence of all the chemical bonding previously mentioned, where the peaks at ~530.2, ~530.8, ~531.6, and ~532.6 represent C=O, MgO, $Mg_3(PO_4)_2$, and O–C=O bonding, respectively. Moreover, the N1s peak did not show subpeaks; rather a single peak was formed of (C_3)–N, which would be contributed by EDTA, as shown in Fig. 5(f). The presence of phosphorus in the inorganic layer was further confirmed through X-ray photoelectron spectroscopy (XPS) analysis, with the P2p peak included in Fig. S2.† The deconvolution of the P2p peak reveals a single oxidation state at ~133.4, corresponding to $Mg_3(PO_4)_2$, indicating that phosphorus is incorporated into the coating as magnesium phosphate.

3.3. Photocatalytic performance

3.3.1. Photocatalytic degradation of rhodamine B and tetracycline. To gain a comprehensive understanding of the photocatalysts, the photocatalytic degradation of the harmful organic dye rhodamine B (Rhd B) and the antibiotic tetracycline (TC) was performed. Consequently, the degradation performance of MgO, NiMOF + EDTA, NiMOF–EDTA, and EDTA–NiMOF was evaluated as illustrated in Fig. 6(a–d) and 7(a–d). The dyes were kept under dark conditions for 60 minutes to ensure adsorption equilibrium before the photocatalytic reaction. The degradation observed during this phase was labeled as "−60 min" in Fig. 6 and 7 for clarity. During this period, minimal degradation of the dyes was observed.

The distinct absorption peak of Rhd B was observed at around 550 nm. The samples were placed in the Rhd B solution and exposed to visible light, and the Rhd B solution was collected after 5 min intervals for a total of 25 min for each sample. The degradation efficiency (η) that was calculated, shown in Fig. 6(e), revealed that the MgO sample degraded only 40.79% of Rhd B solution in 25 min. The ability of the MgO surface to degrade dyes is attributed to its considerably vast surface area, which was a result of the numerous pores present on the surface.[51,52] Furthermore, because the MgO surface offers numerous nucleation sites as well, post treatment could be performed for enhancing the photocatalytic properties. The NiMOF + EDTA and NiMOF–EDTA samples exhibited impressive photodegradation of Rhd B, degrading 90.79% and 94.76% respectively, in 25 min. These impressive results may be attributed to the formation of NiMg LDH, as the unique layered structure, presence of active metal centers, and the overall stability provide significantly more active sites than the MgO surface.[53,54] The presence of both Ni^{2+} and Mg^{2+} may create pathways for efficient electron transfer, improving the overall photocatalytic process. The EDTA–NiMOF sample degraded 99.19% of the Rhd B dye in 25 min, and it is important to notice that 97.67% of the dye was degraded in 20 min, attributing to the fast reaction rate (0.182 min^{-1}) offered by the photocatalyst. This rapid reaction rate for rhodamine B (Rhd B) degradation may be attributed to the inherent characteristics of MOFs, such as their porous structure and extensive surface area, which enhance the accessibility of reactive sites and facilitate efficient

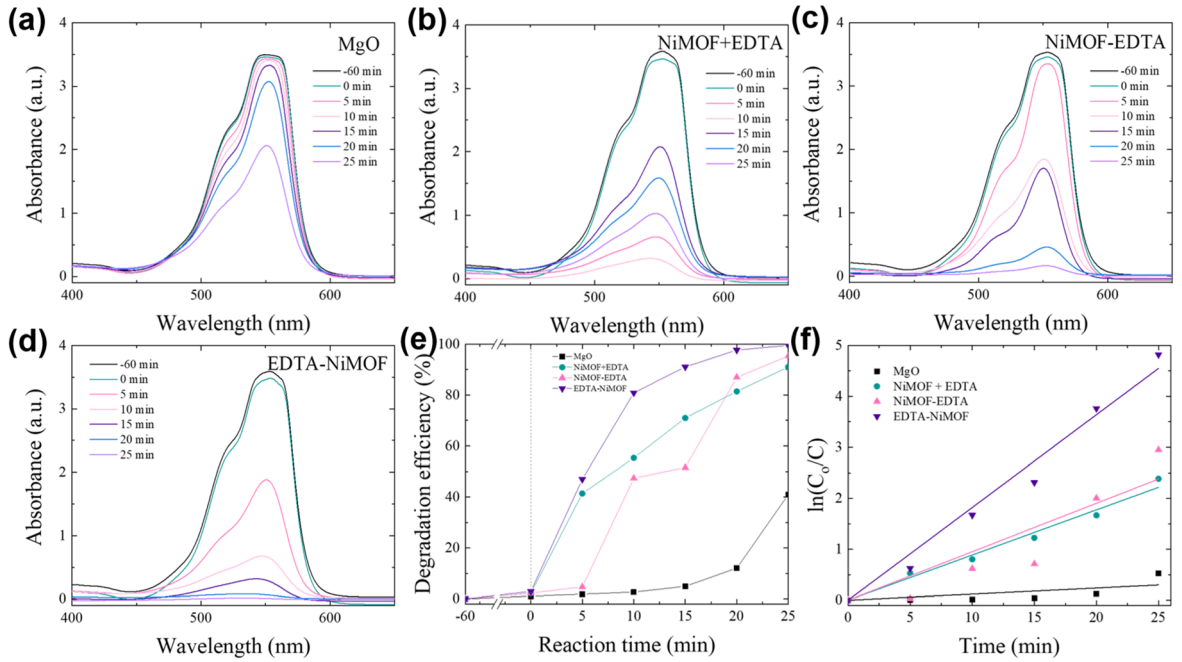

Fig. 6 Photodegradation of rhodamine B using different catalysts: (a) MgO, (b) NiMOF + EDTA, (c) NiMOF–EDTA, and (d) EDTA–NiMOF. (e) Comparison of photodegradation efficiency, and (f) reaction kinetics for all samples.

interaction with pollutant molecules. The reaction kinetics, presented in Fig. 6(f) and Table 1, indicate that all samples adhere to pseudo-first-order kinetics. This conclusion is drawn from the R^2 values, which are closer to 1 for pseudo-first-order kinetics compared to pseudo-second-order kinetics, as shown in Table S1.† This implies that the degradation rate of the samples is directly proportional to the concentration of rhodamine B (Rhd B) in the solution.

Similarly, the effectiveness of the photocatalysts could be extended to the degradation of other contaminants, tetracycline in this case, a commonly used antibiotic that poses significant environmental concerns. Fig. 7(a–d) present the UV-visible

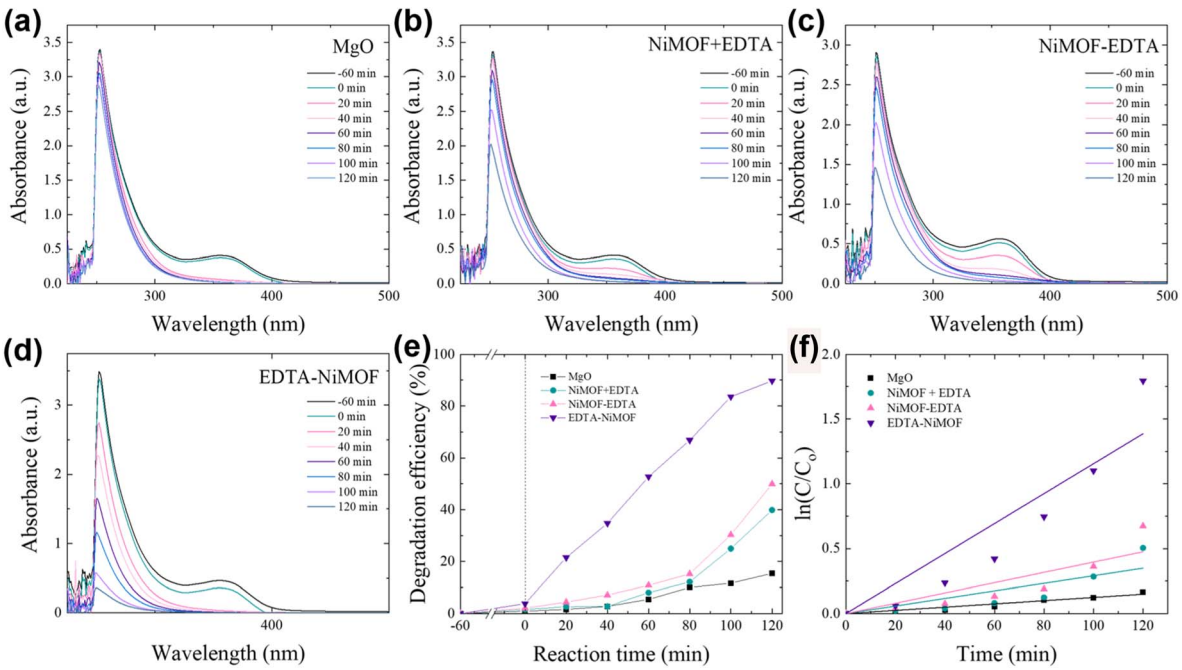

Fig. 7 Photodegradation of tetracycline using various catalysts: (a) MgO, (b) NiMOF + EDTA, (c) NiMOF–EDTA, and (d) EDTA–NiMOF. (e) Comparative analysis of photodegradation efficiency, and (f) reaction kinetics for all samples.

Table 1 Pseudo-first-order reaction kinetics of Rhd B and TC degradation using all samples

	Rhodamine B		Tetracycline	
Sample	Reaction rate (min^{-1})	R^2	Reaction rate (min^{-1})	R^2
MgO	0.01193 ± 0.00375	0.817	0.00124 ± 7.8865×10^{-5}	0.988
NiMOF + EDTA	0.08868 ± 0.00309	0.996	0.00291 ± 4.8789×10^{-4}	0.925
NiMOF–EDTA	0.09516 ± 0.01297	0.956	0.00396 ± 5.92973×10^{-4}	0.938
EDTA–NiMOF	0.182 ± 0.00733	0.995	0.01156 ± 0.00128	0.965

Table 2 Comparison of different photocatalysts reported in the literature for Rhd B degradation

Photocatalyst	Light source	Concentration of rhodamine B (mg L^{-1})	Degradation (%)	Exposure time (min)	Ref
NiFe LDH/CdS	Visible light	20	92.8	120	55
g-C_3N_4/Co/ZnO	Solar light	15 ppm	91.6	120	56
ZnO/g-C_3N_4	500 W xenon lamp	5 ppm	73.0	45	57
0.25%Mo–PCN	350 W visible light	10	99.7	40	58
Z-scheme CeO_2@LDH	50 W visible light	25	91.5	30	59
CdS/Mn-MOF(50)	Visible light	10	98.7	60	60
MgO	Visible light	20	40.7	25	Present work
NiMOF + EDTA	Visible light	20	90.8	25	Present work
NiMOF–EDTA	Visible light	20	94.8	25	Present work
EDTA–NiMOF	Visible light	20	99.2	25	Present work

spectra obtained by degrading tetracycline using every sample. A similar trend to Rhd B degradation was also observed during the degradation of the antibiotic; however it took much longer to degrade as TC is harder to degrade. The degradation was observed over 120 minutes, during which the MgO sample exhibited low degradation efficiency, achieving only 15.28% degradation, as shown in Fig. 7(e), of TC within the given time frame. Moreover, the NiMOF + EDTA and NiMOF–EDTA samples displayed considerably more degradation efficiency 39.66% and 49.07%, respectively. However, the EDTA–NiMOF sample demonstrated exceptionally high degradation efficiency, achieving 90.73% degradation. This remarkable performance can be attributed to the unique characteristics of NiMOF, which provide abundant active sites for tetracycline molecules to adsorb onto the surface. These active sites facilitate the breakdown of tetracycline into smaller intermediate products, which are subsequently degraded into carbon dioxide and water molecules. The reaction kinetic study for TC degradation also indicates that the samples follow the pseudo-first-order reaction kinetics, shown in Fig. 7(f) and Table 1. Moreover, EDTA–NiMOF exhibited the highest reaction rate *i.e.*, 0.01156 min^{-1}. Comparison tables for Rhd B[55–60] and TC[61–66] were constructed to individually assess the performance of the photocatalyst studied in this research against other photocatalysts reported in recent literature. These comparisons are detailed in Table 2 for Rhd B and Table 3 for TC. The results reveal that the EDTA–NiMOF photocatalyst demonstrated comparatively excellent degradation efficiency, suggesting that this work holds significant potential for practical applications in real-world wastewater treatment scenarios.

A mixture of Rhd B and TC solution was degraded using the best sample *i.e.*, EDTA–NiMOF, to see how the reaction would

Table 3 Comparison of various photocatalysts reported in the literature for the TC degradation

Photocatalyst	Light source	Concentration of tetracycline (mg L^{-1})	Degradation (%)	Exposure time (min)	Ref
ZIF-8@NH_2-MIL-125	500 W xenon lamp	20	92.9	120	61
MIL-100(Fe)@PANI	300 W xenon lamp	10	84.0	120	62
CuS@MIL-100(Fe)	Simulated sunlight	40	93.3	240	63
NH_2-MIL-125/Bi_2WO_6	300 W xenon lamp	20	77.8	120	64
NiAl–MoS_4-LDH	Visible light	20	91.0	180	65
FeNi-LDH/Ti_3C_2	300 W xenon lamp	20	94.7	210	66
MgO	Visible light	20	15.2	120	Present work
NiMOF + EDTA	Visible light	20	39.6	120	Present work
NiMOF–EDTA	Visible light	20	49.0	120	Present work
EDTA–NiMOF	Visible light	20	90.7	120	Present work

be affected. The absorption peaks, displayed in Fig. S3(a),† show that the Rhd B peak completely flattens out (99.74% degradation) in about 50 min; however, the TC peak showed approximately 84.50% reduction in the same amount of time. This peculiar behavior suggests that when both molecules are present in the solution, the TC molecules might have a greater affinity to the surface, which causes the Rhd B molecule degradation rate to get slower; hence, more time is required to degrade the Rhd B molecules. Moreover, to investigate the role of hydrogen peroxide (H_2O_2) in the photocatalytic process, additional degradation experiments were conducted without its presence, as shown in Fig. S3(b and c).† The EDTA–NiMOF sample achieved 88.36% degradation of rhodamine B within 25 minutes and 66.50% degradation of tetracycline in 120 minutes, demonstrating significant photocatalytic activity even in the absence of H_2O_2. This confirms that the reaction is not reliant on the Fenton process but is instead driven by the intrinsic photocatalytic properties of the EDTA–NiMOF coating. The addition of H_2O_2 further enhances the reaction by generating additional reactive oxygen species, improving degradation efficiency.

To evaluate the influence of EDTA on the photocatalytic performance of NiMOF-MgO, control experiments were conducted using NiMOF-MgO and EDTA-MgO samples for the degradation of Rhd B and TC, as shown in Fig. S4.† The NiMOF-MgO sample exhibited limited photocatalytic activity, degrading only 10.37% of Rhd B within 25 minutes and 10.42% of TC within 120 minutes. Similarly, the EDTA-MgO sample showed minimal degradation, with 3.03% removal of Rhd B in 25 minutes and 3.50% removal of TC in 120 minutes. These results confirm that NiMOF or EDTA alone on MgO does not significantly enhance photocatalytic performance.

Furthermore, the UV-Vis diffuse reflectance spectroscopy (UV-DRS) spectrum provides insights into the optical properties of the synthesized material. The spectrum exhibits strong absorption in the UV and visible regions, with an absorption edge appearing between 400 and 500 nm, as shown in Fig. S5(a).† This suggests that the material possesses a band gap in the range of approximately 2.5–3.1 eV, making it a potential candidate for visible-light-driven photocatalysis. The extended absorption into the visible region may be attributed to ligand-to-metal charge transfer (LMCT) or defect states, which can enhance photocatalytic performance by improving charge separation efficiency. Fig. S5(b)† presents the Tauc plot for the EDTA–NiMOF sample, confirming its optical band gap energy. The estimated band gap was determined to be 2.83 eV, indicating its ability to absorb visible light efficiently. This value aligns well with the absorption edge observed in the UV-DRS spectrum and suggests that the material has strong potential for visible-light-driven photocatalysis. To highlight the importance of the MgO surface in the formation of functional coatings, the best condition was employed on a bare Mg substrate. However, surface analysis revealed minimal to no deposition, as illustrated in Fig. S6.†

3.3.2. Recyclability and scavenger tests. To ensure the stability of the best photocatalyst, the sample was washed with ethanol and reused for five cycles for each dye separately. Due to the exceptional stability of EDTA–NiMOF, in the fifth cycle, the photocatalyst still degraded 95.2% dye in 25 min, as shown in Fig. 8(a). However, due to the harshness and time-consuming process of TC degradation, an 8.57% drop in performance was observed, as shown in Fig. 8(b). Additionally, surface analysis after five cycles of photocatalysis with both dyes revealed a slight decrease in crystalline integrity, with the scale-like structures showing signs of minor exfoliation. This likely occurs due to the repeated adsorption and desorption of the dye molecules, which can induce stress on the surface layers and gradually disrupt the material's crystalline structure, as seen in Fig. S7.†

To assess the role of specific reactive oxidizing species (ROS) in the photocatalytic degradation of Rhd B and TC, quenchers such as IPA, BQ, and EDTA were used to selectively inhibit hydroxyl radicals ($OH^{\bullet}$), superoxide radicals ($^{\bullet}O_2^-$), and photo-induced holes (h^+), respectively, as illustrated in Fig. 8(c). Fig. S8† presents the UV-Vis absorption spectrum illustrating the effect of scavengers on the degradation of Rhd B and TC. Without scavengers, the EDTA–NiMOF photocatalyst achieved a 99.19% degradation of Rhd B in just 25 minutes, while TC degradation reached 90.73% in 120 minutes. The efficiency of the degradation process decreased with the addition of each

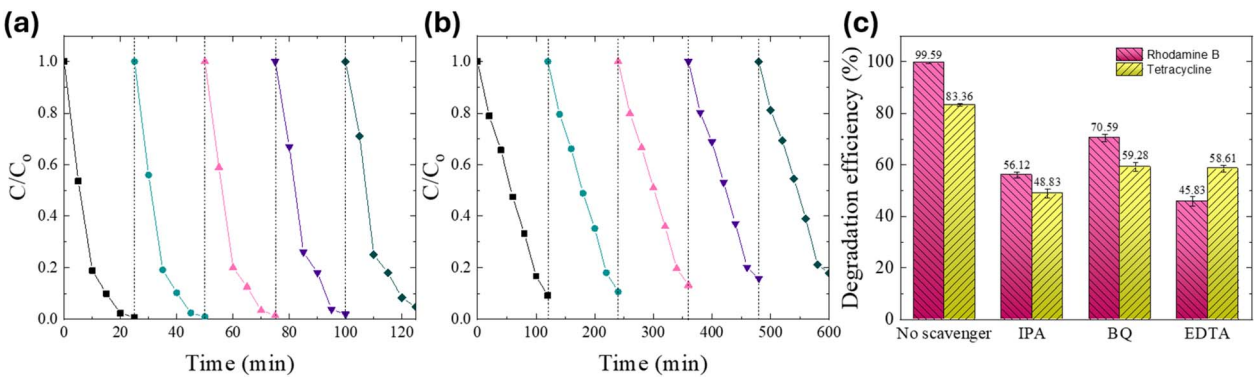

Fig. 8 Cyclability of EDTA–NiMOF for five cycles for (a) Rhd B and (b) TC. (c) Scavenger test evaluation for both dyes to understand the effects of the reactive oxidizing agent.

scavenger, indicating the significant role of each ROS in the photocatalytic process. For Rhd B, the degradation efficiency dropped from 99.19% to 56.12% with the addition of IPA, suggesting effective trapping of $OH^{\bullet}$ radicals. Meanwhile, the degradation efficiency decreased to 70.59% with the addition of BQ, indicating a lower contribution from $^{\bullet}O_2^-$ radicals. A significant drop in degradation was observed when EDTA as a scavenger was used, decreasing the efficiency to 45.83%, implying that the main contributor in the photocatalytic process of Rhd B was h^+. Furthermore, in the case of TC, IPA displays the highest quenching, implying that $OH^{\bullet}$ radicals are the most reactive species during the photocatalysis of TC, whereas the quenching that was observed using BQ and EDTA was 59.28% and 58.61% respectively, indicating that the $^{\bullet}O_2^-$ and h^+ had a lower but almost equal effect on the photocatalytic degradation.

3.3.3. Photodegradation mechanism. The photocatalytic degradation mechanism for Rhd B and TC using EDTA–NiMOF as a photocatalyst operates in a similar sequential manner. The process begins with the absorption of photons with energy comparable to the band gap of the photocatalyst. This photon absorption excites electrons, causing them to move from the valence band to the conduction band, as illustrated in Fig. 9. The induced charges resulting from electron excitation target the initiator (H_2O_2), generating highly reactive hydroxyl radicals ($OH^{\bullet}$). Additionally, these charges react with H_2O and O_2 molecules, producing more $OH^{\bullet}$ and hydroperoxide ($HOO^{\bullet}$), as depicted in eqn (13)–(18). These reactive species then attack the dye molecules, breaking them down into intermediate compounds. Subsequently, the radicals continue to degrade these intermediates, ultimately converting them into water and carbon dioxide.

$$\text{Catalyst} + \text{light source (hv)} \rightarrow \text{Catalyst } (h^+)_{VB} + \text{Catalyst } (e^-)_{CB} \quad (13)$$

$$\text{Catalyst } (e^-)_{CB} + H_2O_2 \rightarrow OH^{\bullet} + OH^{1-} \quad (14)$$

$$\text{Catalyst } (h^+)_{VB} + OH^{1-} \rightarrow OH^{\bullet} \quad (15)$$

$$\text{Catalyst } (e^-)_{CB} + O_2 \rightarrow O_2^{1-} \quad (16)$$

$$\text{Catalyst } (h^+)_{VB} + H_2O \rightarrow OH^{\bullet} + H^{1+} \quad (17)$$

$$O_2^{1-} + H^+ \rightarrow HOO^{\bullet} \quad (18)$$

The superior photocatalytic efficiency of the EDTA–NiMOF sample is primarily due to its highly crystalline MOF architecture, which offers an abundance of active sites, enhanced light-harvesting capability, and efficient separation of photo-generated charge carriers. In contrast, the LDH structures, displayed by NiMOF + EDTA and NiMOF–EDTA, demonstrate reduced photocatalytic activity, stemming from their inherently lower surface area and less crystalline nature, particularly due to the formation of smaller, less well-defined flakes. The charge transfer within the LDH is also less efficient, as the LDH structure formed by the sequential addition of EDTA comprises two divalent metal ions (Ni^{2+} and Mg^{2+}) rather than the typical combination of divalent and trivalent metal ions found in conventional LDHs.[67,68] This deviation disrupts the conventional electronic structure, leading to suboptimal charge transport and, consequently, lower photocatalytic performance. Furthermore, the XRD analysis revealed that the intensity of the LDH peak in the NiMOF + EDTA sample was significantly lower compared to that in the NiMOF–EDTA sample. This suggests that the LDH layer formed on the NiMOF + EDTA surface is both non-uniform and thinner than the more robust coating observed in the NiMOF–EDTA sample. The reduced peak intensity is indicative of lower crystallinity and less extensive layer formation, which likely contributes to the diminished photocatalytic performance of the NiMOF + EDTA sample relative to NiMOF–EDTA. Thus, the order of EDTA incorporation is crucial in dictating whether the resulting material adopts a MOF or LDH structure, significantly impacting its photocatalytic properties.

3.4. Computational analysis

The bonding structure of the compounds *i.e.*, TPA and EDTA, and their complex with nickel were studied using the DFT

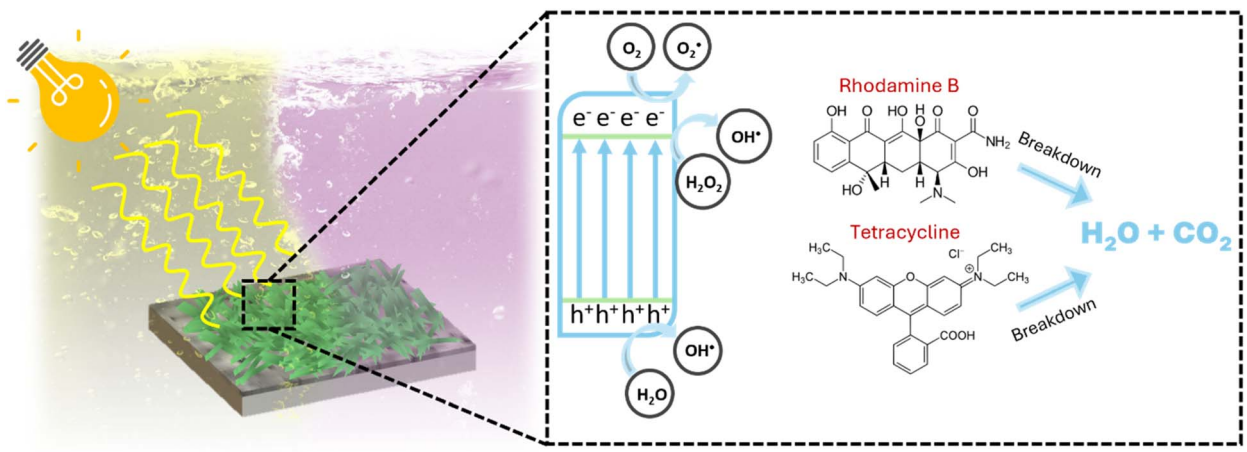

Fig. 9 Photocatalytic degradation mechanism of EDTA–NiMOF.

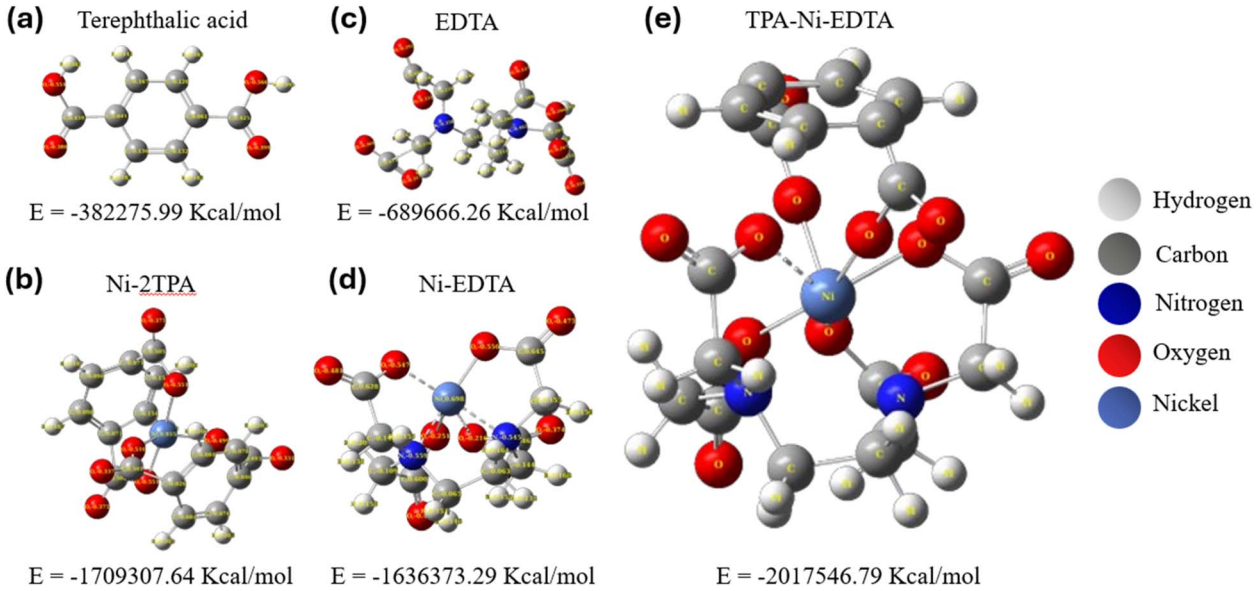

Fig. 10 Optimized structure and the optimized energy of (a) terephthalic acid (TPA), (b) Ni–2TPA, (c) EDTA, (d) Ni–EDTA, and (e) TPA-Ni–EDTA.

method. Furthermore, their optimized energies were also calculated, to gain comprehensive knowledge about the likelihood of the reactions occurring during the synthesis of the coating. The optimized structures and their respective energies are presented in Fig. 10(a–e) and Table S2,† respectively. The bonding energy can be calculated using the following formulae:

$$E_B\ (\text{TPA–Ni}) = (E_{\text{Ni–2TPA}} - E_{\text{2TPA}} - E_{\text{Ni}})/2 = 743.77\ \text{kcal mol}^{-1} \quad (19)$$

$$E_B\ (\text{EDTA–Ni}) = E_{\text{Ni–EDTA}} - E_{\text{EDTA}} - E_{\text{Ni}} = -463.82\ \text{kcal mol}^{-1} \quad (20)$$

$$E_B\ (\text{TPA \& EDTA–Ni}) = E_{\text{TPA–Ni–EDTA}} - E_{\text{EDTA}} - E_{\text{TPA}} - E_{\text{Ni}} = 638.67\ \text{kcal mol}^{-1} \quad (21)$$

Calculating these bonding energies was crucial for understanding the formation of NiMg LDH and explaining why the NiMOF + EDTA sample exhibited less deposition of NiMg LDH. Initially, during the synthesis of NiMOF + EDTA, it is predicted that a complex involving TPA, EDTA, and Ni would form. However, the bonding energy of this complex is the highest among the ones studied, which suggests that its formation is less favorable. This would hinder the formation of NiMg LDH, explaining the lower intensity of the NiMg LDH XRD peak observed in the NiMOF + EDTA sample, as discussed in Section 3.2.

Conversely, when EDTA was introduced in the second step rather than being combined with TPA from the beginning, the reactions proposed in eqn (9)–(12) were more likely to occur. The bonding energy of EDTA with nickel is lower compared to that of TPA with nickel, as shown using the calculations in eqn (19) and (20). This indicates that nickel has a stronger affinity for binding with EDTA than with TPA. As a result, nickel preferentially forms a complex with EDTA, releasing TPA, which aligns with the proposed reaction mechanism for the formation of NiMg LDH. Therefore, the sequence of EDTA addition plays a critical role in determining the type of complex formed on the surface. If EDTA is added simultaneously with NiMOF, the result is a less uniform, thinner layer of LDH. However, if EDTA is added after the formation of NiMOF, it leads to the formation of a more uniform and stable LDH layer.

For the EDTA–NiMOF sample, surface visualization and optimization were performed on the MgO substrate, and this was compared with the surface visualization of NiMg LDH on MgO. The comparison was aimed at understanding the differences between these two structures on the MgO surface. Starting with the NiMg LDH, as shown in Fig. 11(a and b), the visualization reveals hydrogen bonding interactions between the MgO surface and the hydrogen atoms in the NiMg LDH structure. In contrast, for the EDTA–NiMOF system, the EDTA first forms a complex with the MgO surface, establishing strong hydrogen bonds with the numerous hydrogen atoms present. Once the MgO surface is functionalized with EDTA, the subsequent addition of NiMOF results in nickel atoms binding to the oxygen atoms abundant in the EDTA molecule. These nickel atoms then interact with terephthalic acid (TPA) to form a stable NiMOF coating on the surface, as illustrated in Fig. 11(c and d).

The EDTA–NiMOF complex exhibits significantly greater stability compared to NiMg LDH, primarily due to the robust EDTA–MgO interaction. Additionally, the formation of the NiMOF layer on the surface provides a higher density of active sites, which is beneficial for photocatalysis. Moreover, the adsorption energy of the EDTA–NiMOF complex with Rhd B and TC was optimized and calculated, as displayed in Fig. S9.† The significantly lower adsorption energy of the complex with Rhd B ($E_{ads} = -168.8$ kcal mol^{-1}) compared to the adsorption energy with TC ($E_{ads} = -40.1$ kcal mol^{-1}) indicates that less energy is

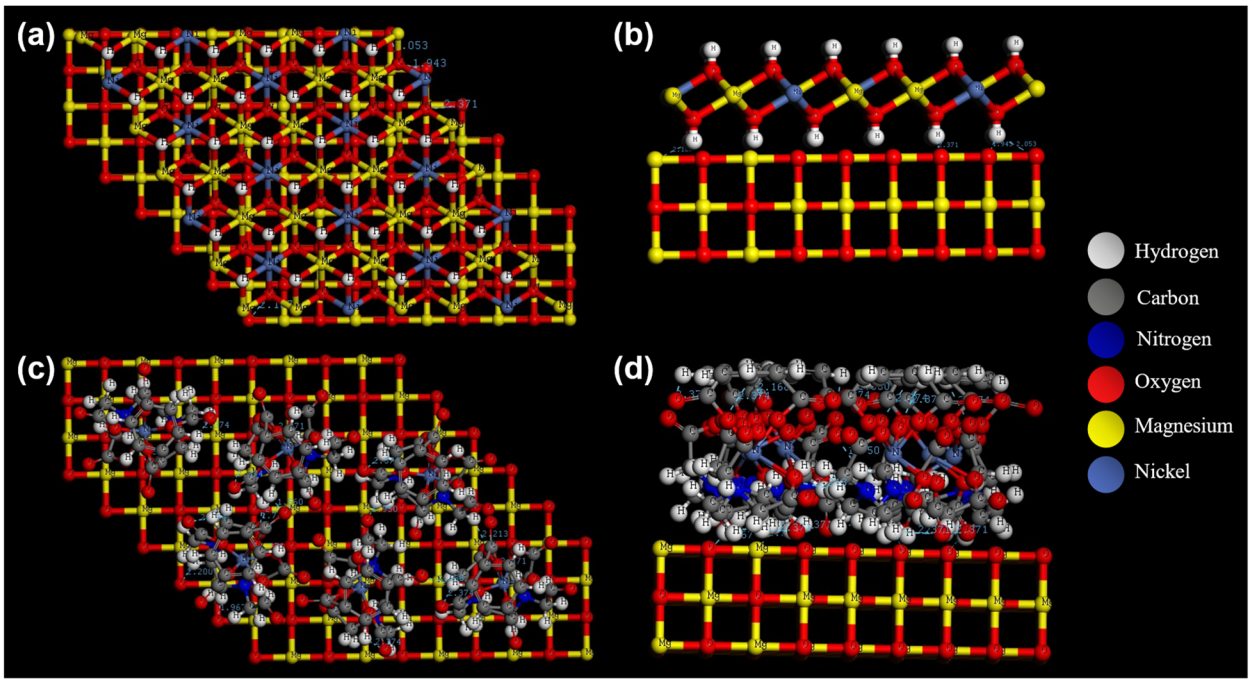

Fig. 11 Surface modelling and optimization of MgO with (a and b) NiMg LDH and (c and d) EDTA–Ni–TPA.

required to adsorb Rhd B molecules. This suggests a stronger interaction between the EDTA–NiMOF complex and Rhd B, potentially leading to more efficient photocatalytic degradation of the dye in comparison to TC.

4. Conclusions

The sequential addition of EDTA to NiMOF was systematically studied, revealing intriguing behavior during the synthesis process. When EDTA was introduced either simultaneously with NiMOF or in a subsequent step on a MgO surface, a layer of NiMg LDH was formed. However, when EDTA was first applied to the MgO surface before adding NiMOF, a fully adhered and functional NiMOF coating was successfully developed. To demonstrate the effectiveness of these coatings, photocatalytic degradation of Rhd B and TC was performed. The EDTA–NiMOF sample, characterized by its numerous active sites within the hybrid complex, achieved remarkable degradation efficiencies, with 99.2% of Rhd B degraded within 25 minutes and 90.7% of TC within 120 minutes. In contrast, samples exhibiting an LDH structure, such as NiMOF + EDTA and NiMOF–EDTA, displayed significantly lower photocatalytic activity compared to the EDTA–NiMOF sample. Additionally, the EDTA–NiMOF coating demonstrated excellent stability, maintaining high degradation efficiency over five cycles without significant loss in performance.

Data availability

The data that support the findings of this study are available from the corresponding author upon reasonable request.

Conflicts of interest

There are no conflicts to declare.

Acknowledgements

This work was supported by the National Research Foundation of Korea (NRF) funded by the Korean government (MSIT) (No. 2022R1A2C1006743).

References

1 M. A. Khan, A. R. Safira, M. Aadil and M. Kaseem, *J. Magnesium Alloys*, 2024, **12**(2), 586–607.
2 B. V. K. J. Schmidt, *Macromol. Rapid Commun.*, 2020, **41**, 1900333.
3 P. He, H. Lan, H. Bai, Y. Zhu, Z. Fan, J. Liu, L. Liu, R. Niu, Z. Dong and J. Gong, *Appl. Catal., B*, 2023, **337**, 123001.
4 M. Aadil, M. A. Khan, S. A. Repycha and M. Kaseem, *Nano Mater. Sci.*, 2024, **6**(5), 548–564.
5 M. Kaseem, K. Ramachandraiah, S. Hossain and B. Dikici, *Nanomaterials*, 2021, **11**(2), 536, DOI: **10.3390/nano11020536**.
6 M. Kaseem, A. R. Safira and A. Fattah-alhosseini, *J. Magnesium Alloys*, 2024, **12**(1), 267–280.
7 W.-Q. Wu, D. Chen, R. A. Caruso and Y.-B. Cheng, *J. Mater. Chem. A*, 2017, **5**, 10092–10109.
8 S. Brittman, G. W. P. Adhyaksa and E. C. Garnett, *MRS Commun.*, 2015, **5**, 7–26.
9 W. Li, Z. Wang, F. Deschler, S. Gao, R. H. Friend and A. K. Cheetham, *Nat. Rev. Mater.*, 2017, **2**, 16099.
10 J. Tang, C. Su and Z. Shao, *Small Methods*, 2021, **5**, 2100945.

11 S. Jin, H. Chen, K. Pan, R. Li, X. Ma, R. Yuan, X. Meng and H. He, *Talanta*, 2024, **270**, 125557.
12 B. Zhang, Y. Zheng, T. Ma, C. Yang, Y. Peng, Z. Zhou, M. Zhou, S. Li, Y. Wang and C. Cheng, *Adv. Mater.*, 2021, **33**, 2006042.
13 W. Fan, X. Zhang, Z. Kang, X. Liu and D. Sun, *Coord. Chem. Rev.*, 2021, **443**, 213968.
14 T. Jia, Y. Gu and F. Li, *J. Environ. Chem. Eng.*, 2022, **10**, 108300.
15 D. H. Hong, H. S. Shim, J. Ha and H. R. Moon, *Bull. Korean Chem. Soc.*, 2021, **42**, 956–969.
16 H.-R. Tian, Z. Zhang, S.-M. Liu, T.-Y. Dang, X.-H. Li, Y. Lu and S.-X. Liu, *J. Mater. Chem. A*, 2020, **8**, 12398–12405.
17 F. Huang, M. Humayun, G. Li, T.-T. Fan, W.-L. Wang, Y.-L. Cao, A. Nikiforov, C.-D. Wang and J. Wang, *Rare Met.*, 2024, **43**, 3161–3172.
18 Z. S. Yuan, J. X. Zou, X. L. Zhao, J. Y. Shi, C. S. Guo and M. Yan, *J. Mater. Sci. Technol.*, 2023, **166**, 86–97.
19 S. Mallakpour, E. Nikkhoo and C. M. Hussain, *Coord. Chem. Rev.*, 2022, **451**, 214262.
20 H. D. Lawson, S. P. Walton and C. Chan, *ACS Appl. Mater. Interfaces*, 2021, **13**, 7004–7020.
21 S. S. Sankar, G. Keerthana, K. Manjula, J. H. Sharad and S. Kundu, *Inorg. Chem.*, 2021, **60**, 4034–4046.
22 A. R. Safira, A. H. Alluhayb, M. Aadil, M. Alkaseem, A. Fattah-alhosseini and M. Kaseem, *Composites, Part B*, 2024, **284**, 111710.
23 H. Boumeriame, E. S. Da Silva, A. S. Cherevan, T. Chafik, J. L. Faria and D. Eder, *J. Energy Chem.*, 2022, **64**, 406–431.
24 D. Fang, L. Huang, J. Fan, H. Xiao, G. Wu, Y. Wang, Z. Zeng, F. Shen, S. Deng and F. Ji, *Chem. Eng. J.*, 2022, **441**, 136057.
25 F. Hajargasht, S. Borhani, V. Safarifard and M. Moradi, *Synth. Met.*, 2022, **291**, 117164.
26 L. D. Silva Neto, A. F. Silva, J. T. Freire and L. Meili, in *Advanced Materials for Sustainable Environmental Remediation*, ed. D. Giannakoudakis, L. Meili and I. Anastopoulos, Elsevier, 2022, doi: DOI: **10.1016/B978-0-323-90485-8.00016-3**, pp. 301–323.
27 S. Rana, A. Kumar, C. W. Lai, G. Sharma and P. Dhiman, *Chemosphere*, 2024, **356**, 141800.
28 Y. Zhao, X. Jia, G. I. N. Waterhouse, L.-Z. Wu, C.-H. Tung, D. O'Hare and T. Zhang, *Adv. Energy Mater.*, 2016, **6**, 1501974.
29 P. Miao, J. Zhao, R. Shi, Z. Li, Y. Zhao, C. Zhou and T. Zhang, *ACS ES&T Eng.*, 2022, **2**, 1088–1102.
30 L. Zhang, J. Liang, L. Yue, K. Dong, J. Li, D. Zhao, Z. Li, S. Sun, Y. Luo, Q. Liu, G. Cui, A. Ali Alshehri, X. Guo and X. Sun, *Nano Res. Energy.*, 2022, **1**, 9120028.
31 G. Xia, Y. Zheng, Z. Sun, S. Xia, Z. Ni and J. Yao, *Environ. Sci. Pollut. Res.*, 2022, **29**, 39441–39450.
32 R. Gabriel, S. H. V. d. Carvalho, J. L. d. S. Duarte, L. M. T. M. Oliveira, D. A. Giannakoudakis, K. S. Triantafyllidis, J. I. Soletti and L. Meili, *Appl. Catal., A*, 2022, **630**, 118470.
33 N. Wen, Y. Su, W. Deng, H. Zhou, M. Hu and B. Zhao, *Chem. Eng. J.*, 2022, **438**, 135570.
34 E. Hafer, U. Holzgrabe, K. Kraus, K. Adams, J. M. Hook and B. Diehl, *Magn. Reson. Chem.*, 2020, **58**, 653–665.
35 M. Shukla, B. Baksi, S. P. Mohanty, B. Mahanty, A. Mansi, E. R. Rene and S. K. Behera, *Prog. Org. Coat.*, 2022, **165**, 106704.
36 K. Zhang, Z. Dai, W. Zhang, Q. Gao, Y. Dai, F. Xia and X. Zhang, *Coord. Chem. Rev.*, 2021, **434**, 213809.
37 A. Hassan, M. Mahmoud, B. S. Bageri, M. S. Aljawad, M. S. Kamal, A. A. Barri and I. A. Hussein, *Energy Fuels*, 2020, **34**, 15593–15613.
38 L. P. Kowtharapu, N. K. Katari, C. A. Sandoval, V. K. Rekulapally and S. B. Jonnalagadda, *ACS Omega*, 2022, **7**, 34098–34108.
39 S.-H. Chang, Y.-J. Chen, H.-J. Tseng, H.-I. Hsiao, H.-J. Chai, K.-C. Shang, C.-L. Pan and G.-J. Tsai, *Membranes*, 2021, **11**, 852.
40 J. Khan, N. Shakeel, S. Alam, M. Z. Iqbal, Z. Ahmad and K. Yusuf, *Electrochim. Acta*, 2024, **486**, 143970.
41 Y. Wu, X. Song, J. Zhang, S. Xu, N. Xu, H. Yang, Y. Miao, L. Gao, J. Zhang and G. Xiao, *Chem. Eng. Res. Des.*, 2018, **140**, 273–282.
42 F. Meng, Y. Liu, K. Shi, J. Zhou, F. Yan and J. Wang, *ACS Omega*, 2024, **9**(31), 33594–33605.
43 R. Devendiran, S. Chinnaiyan, R. Mohanty, R. Giriprasath, S. Singaravelu, L. Sobhana S S and U. Sivagnanam, *J. Biomater. Tissue Eng.*, 2014, **4**, 430–438.
44 F. Altaf, R. Gill, P. Bocchetta, R. Batool, M. U. Hameed, G. Abbas and K. Jacob, *Energies*, 2021, **14**, 3578.
45 Y. Kurniawan, M. Fahmi and L. Yuliati, *IOP Conf. Ser.:Mater. Sci. Eng.*, 2020, **833**, 012018.
46 M. Zeraati, V. Alizadeh, P. Kazemzadeh, M. Safinejad, H. Kazemian and G. Sargazi, *J. Porous Mater.*, 2022, **29**, 257–267.
47 X. Hang, Y. Xue, Y. Cheng, M. Du, L. Du and H. Pang, *Inorg. Chem.*, 2021, **60**, 13168–13176.
48 H. Chu, Y. Zhu, T. Fang, J. Hua, S. Qiu, H. Liu, L. Qin, Q. Wei, Y. Zou, C. Xiang, F. Xu and L. Sun, *Sustainable Energy Fuels*, 2020, **4**, 337–346.
49 S. Karimi, F. Meshkani, M. Rezaei and A. Rastegarpanah, *Powder Technol.*, 2024, **443**, 119896.
50 M. A. Khan, A. R. Safira and M. Kaseem, *J. Mater. Chem. A*, 2024, **12**, 3411–3433.
51 S. Stojadinović, N. Tadić, N. Radić, B. Grbić and R. Vasilić, *Surf. Coat. Technol.*, 2017, **310**, 98–105.
52 S. Stojadinović and N. Radić, *Metals*, 2024, **14**(3), 366, DOI: **10.3390/met14030366**.
53 M. Aadil, T. T. Thanaa, M. Alkaseem and M. Kaseem, *Adv. Compos. Hybrid Mater.*, 2024, **8**, 34.
54 M. Aadil, A. R. Safira, A. Fattah-alhosseini, M. Alkaseem and M. Kaseem, *J. Magnesium Alloys*, 2024, **12**, 3729–3743.
55 G.-Q. Zhao, J. Zou, X. Long, J. Hu and F.-P. Jiao, *J. Alloys Compd.*, 2022, **923**, 166460.
56 H. Leelavathi, R. Muralidharan, N. Abirami, S. Tamizharasan, S. Sankeetha, A. Kumarasamy and R. Arulmozhi, *Colloids Surf., A*, 2023, **656**, 130449.
57 R. Uma, K. Ravichandran, S. Sriram and B. Sakthivel, *Mater. Chem. Phys.*, 2017, **201**, 147–155.

58 K.-L. Wang, H.-M. Zhao, Y. Li, T. Sun and B. Xue, *Appl. Surf. Sci.*, 2020, **528**, 146931.
59 C. Yang, G. Zhang, Y. Meng, G. Pan, Z. Ni and S. Xia, *J. Hazard. Mater.*, 2021, **408**, 124908.
60 C.-Y. Zhu, M.-T. Shen, M.-J. Qi, Y.-Y. Zhao, Z. Xu, P. Li, J. Ru, W. Gao and X.-M. Zhang, *Dyes Pigm.*, 2023, **219**, 111607.
61 B. Xue, C. Yang, M. Chang and D. Liu, *J. Alloys Compd.*, 2024, **973**, 172850.
62 D.-D. Chen, X.-H. Yi, C. Zhao, H. Fu, P. Wang and C.-C. Wang, *Chemosphere*, 2020, **245**, 125659.
63 L. Shu, X.-F. Zhang, S. Yang, J. Qiu and J. Yao, *Sep. Purif. Technol.*, 2024, **334**, 125971.
64 S. Yin, Y. Chen, Q. Hu, M. Li, Y. Ding, J. Di, J. Xia and H. Li, *Res. Chem. Intermed.*, 2020, **46**, 3311–3326.
65 Z. Zhang, H. Zhao, X. Ma, N. Zhang, Z. Meng, Y. Wang, M. Zhao, H. Liu and Q. Zhang, *Sep. Purif. Technol.*, 2024, **337**, 126388.
66 L. Yang, L. Li, Z. Liu, C. Lai, X. Yang, X. Shi, S. Liu, M. Zhang, Y. Fu, X. Zhou, H. Yan, F. Xu, D. Ma and C. Tang, *Chemosphere*, 2022, **294**, 133736.
67 Z. Yang, F. Wang, C. Zhang, G. Zeng, X. Tan, Z. Yu, Y. Zhong, H. Wang and F. Cui, *RSC Adv.*, 2016, **6**, 79415–79436.
68 M. A. Khan, A. Fattah-alhosseini and M. Kaseem, *Inorg. Chem. Commun.*, 2023, **153**, 110739.